Article ID: 1000-7032(2025)07-1241-08

Erbium-sensitized Broadband Near-infrared Luminescence in Nanoparticles

ZHAO Yu, HUANG Jinshu, LU Kecen, HUANG Mengyue, ZHOU Bo*

(*State Key Laboratory of Luminescent Materials and Devices, South China University of Technology, Guangzhou* 510641, *China*)

* *Corresponding Author, E-mail: zhoubo@scut. edu. cn*

Abstract: Broadband near-infrared (NIR) luminescent materials have shown great promise in applications such as optical communication, biomedicine, and optoelectronic devices. However, the current research is focused on phosphors and glasses, and it is important to develop broadband NIR luminescent nanomaterials. Here, we report an erbium-sensitized core-shell nanocrystal design for broadband NIR emission. Based on the structural design with suitable dopings of Tm^{3+} and Ho^{3+}, the broadband NIR emission covering 1. 5-2. 1 μm region is achieved under 980 nm and 808 nm excitations. Moreover, the emission intensity is further enhanced by introducing Yb^{3+} and Nd^{3+} into the sample, respectively, and the energy transfer processes between them are systematically discussed. Our results present a novel approach for developing broadband NIR luminescent materials and devices.

Key words: broadband near-infrared luminescence; lanthanide ions; core-shell structure; energy transfer

CLC number: O482. 31 **Document code**: A

DOI: 10. 37188/CJL. 20250055 **CSTR**: 32170. 14. CJL. 20250055

铒敏化的纳米粒子宽带近红外发光

赵 宇, 黄今殊, 陆柯岑, 黄梦月, 周 博*

(华南理工大学 发光材料与器件全国重点实验室, 广东 广州 510641)

摘要: 宽带近红外发光材料在光通信、生物医学、光电器件等领域具有重要应用。目前,宽带红外发光研究主要集中在荧光粉、玻璃等材料体系,开发宽带近红外纳米发光材料对于推动红外发光材料应用基础研究具有重要意义。本文报道了一种铒基质敏化的近红外宽带发光核壳结构纳米晶。通过核壳纳米结构设计掺杂 Tm^{3+}和 Ho^{3+},实现了铒基质敏化的1.5~2.1 μm(980 nm和808 nm激发)高效宽带近红外发光。通过分别引入 Yb^{3+}和 Nd^{3+},进一步提升了近红外发光强度,分析了离子之间的能量传递过程。上述结果为宽带近红外发光材料和器件开发提供了新思路与材料基础。

关 键 词: 宽带近红外发光; 镧系离子; 纳米粒子; 核壳结构; 能量传递

1 Introduction

Recently, broadband near-infrared (NIR) luminescence has received extensive attention in many fields including optical communication, bioimaging, infrared sensing and photoelectric devices due to its small scattering loss, deep penetration and high energy conversion efficiency[1-9]. The early research showed that lanthanide ions are good candidate for NIR emissions. For example, Er^{3+}, Tm^{3+} and Ho^{3+} are capable of generating 1. 5 μm ($^4I_{13/2}\rightarrow{}^4I_{15/2}$ transition), 1. 8 μm ($^3F_4\rightarrow{}^3H_6$ transition) and 2. 0 μm

收稿日期: 2025-02-28; **修订日期**: 2025-03-16
基金项目: 国家自然科学基金(52272151)
Supported by National Natural Science Foundation of China (52272151)

($^5I_7 \rightarrow {}^5I_8$ transition) emissions respectively, in sensitizer-activator codoped systems[10-12]. However, these materials are usually concentrated on phosphors and glass materials with limitations such as narrow emission spectrum and big samples size. In contrast, the luminescent nanoparticles can achieve broadband spectral emission through the rational design of the structure and surface modification of nanoparticles. Moreover, they have a flexible preparation process, making it convenient to prepare various miniaturized optical devices and sensors[13-18]. At present, the current investigation of lanthanide doped nanoparticles on NIR luminescence is mainly focused on single doping of Er^{3+} (1.5 μm) and Tm^{3+} (1.8 μm)[7,19-20]. It has remained a challenge to realize broadband NIR luminescence covering 1.5–2.1 μm. On the other hand, exploring more excitation wavelengths is also important in addition to the regular 980 nm[21]. Recent research has demonstrated that Er^{3+} possesses a greater variety of excitation wavelengths and can also serve as a sensitizer to activate the NIR emissions of other lanthanides[21-22]. Therefore, it is highly desirable to achieve broadband NIR emissions in the nanoparticles with rational structure design and selection of emitters.

Here we describe a conceptual model to realize broadband NIR luminescence from erbium-sensitized nanoparticles as illustrated in Fig. 1(a). In this design, Er^{3+} works as sensitizer to harvest the 1 530, 980, 808 nm irradiation energy *via* its $^4I_{13/2} \leftarrow {}^4I_{15/2}$, $^4I_{11/2} \leftarrow {}^4I_{15/2}$, $^4I_{9/2} \leftarrow {}^4I_{15/2}$ absorption transitions (Fig. 1(b)). Notably, the small energy gap between Er^{3+} and Tm^{3+}/Ho^{3+} boost energy transfers between them with resultant NIR luminescence at 1.5 μm (Er^{3+}), 1.8 μm (Tm^{3+}) and 2.0 μm (Ho^{3+}) under multi-wavelength excitations. We also establish a core-shell-shell nanostructure to enhance broadband NIR in which Tm^{3+} and Ho^{3+} are spatially separated to suppress unwanted energy interactions. More importantly, the Yb^{3+} and Nd^{3+} are designed to enhance the broadband NIR emissions under 980 nm and 808 nm excitations, respectively. Such broadband NIR emission from lanthanide doped nanoparticles holds substantial importance in fields such as energy conversion, multimodal diagnosis and treatment and high-dimensional encryption.

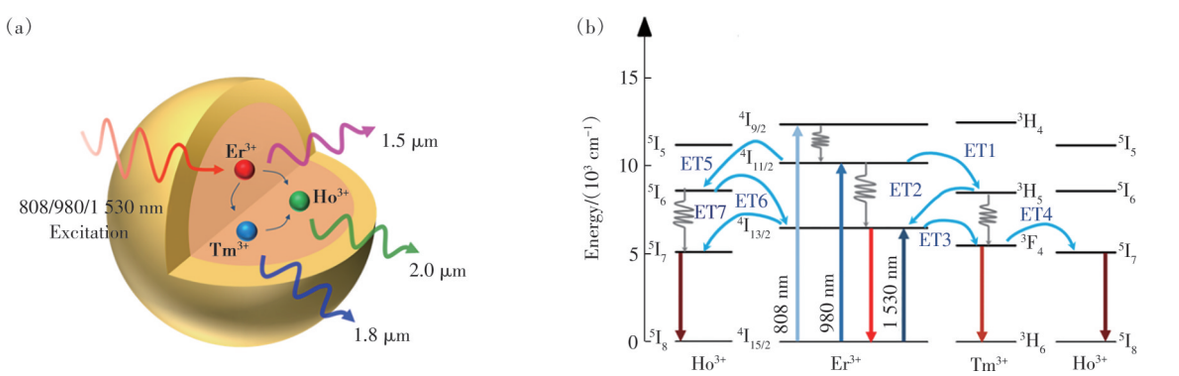

Fig. 1 (a) Schematic of erbium sensitized $NaErF_4$:Tm/Ho@$NaYF_4$ core-shell nanostructure. Energy transfer processes for infrared emissions. ET1–7 represent Er^{3+} ($^4I_{11/2}$) → Tm^{3+} ($^3H_5$), Tm^{3+} ($^3H_5$) → Er^{3+} ($^4I_{13/2}$), Er^{3+} ($^4I_{13/2}$) → Tm^{3+} ($^3F_4$), Tm^{3+} ($^3F_4$) → Ho^{3+} ($^5I_7$), Er^{3+} ($^4I_{11/2}$) → Ho^{3+} ($^5I_6$), Ho^{3+} ($^5I_6$) → Er^{3+} ($^4I_{13/2}$), and Er^{3+} ($^4I_{13/2}$) → Ho^{3+} ($^5I_7$), respectively

2 Experiment

2.1 Materials

Lanthanide chemical reagents, including erbium acetate hydrate (99.9%), thulium acetate hydrate (99.9%), holmium acetate hydrate (99.9%), ytterbium acetate hydrate (99.99%), yttrium acetate hydrate (99.9%), neodymium acetate hydrate (99.9%), oleic acid (>90%), 1-octadecene (>90%), and cyclohexane, were all purchased from Sigma-Aldrich. Ammonium fluoride and sodium hydroxide (NaOH, ≥98%) were obtained from Alfa Aesar. Ethanol was purchased from Aladdin.

2.2 Synthesis of Nanoparticles

The nanoparticles were synthesized using high-temperature co-precipitation and thermal decomposition methods with some modifications. First, 3.5 mL of

oleic acid (OA), 6.5 mL of 1-octadecene (ODE), and 0.4 mmol of rare-earth acetate were added to a 50 mL two-neck flask. The mixture was heated at 150 ℃ for 45 min and cooled down to the room temperature. Next, the temperature was raised to 50 ℃, and 2 mL of 0.5 mol/L sodium hydroxide (NaOH) solution and 4 mL of 0.4 mol/L ammonium fluoride (NH_4F) solution were added. The mixture was stirred for 35 min, followed by heating to 100 ℃ under vacuum to remove methanol. Finally, the mixture was heated at 290 ℃ under an argon flow for 1.5 h, followed by cooling down to room temperature. The resulting core nanoparticles were collected by centrifugation, washed with ethanol for two times, and finally dispersed in cyclohexane.

The shell was prepared using the thermal decomposition method. 5 mL of OA, 5 mL of ODE and a trifluoroacetate solution were added to a 50 mL two-neck flask. The mixture was heated at 120 ℃ for 30 min. After cooling to room temperature, the synthesized nanocrystal core solution was added. The mixture was heated to 110 ℃ under vacuum, followed by stirring for 15 min. Finally, the mixture was heated at 300 ℃ under an argon flow for 40 min, resulting in a 1 mol/L core-shell nanoparticle solution. Other core-shell based nanoparticles were prepared using the similar methods by using specific lanthanide precursors and seeds.

2.3 Characterization

The transmission electron microscopy (TEM) images were obtained using a JEOL JEM-1400 plus microscope operating at 120 kV. X-ray diffraction (XRD) patterns were collected using a Philips PW 1 830 X-ray powder diffractometer. Fluorescence spectra were measured using a Zolix fluorescence spectrometer (OmniFluo 900), coupled with 808, 980, 1 530 nm lasers. The decay curves and quantum yield were measured using the same fluorescence spectrometer .

3 Results and Discussion

At first, a series of $NaErF_4$: Tm (1%–10%) @ $NaYF_4$ core-shell nanoparticles were synthesized (Fig. 2(a) and Fig. S1–2), showing a uniform spherical morphology and monodisperse characteristic with average sizes of 21.2–25.8 nm. The percent

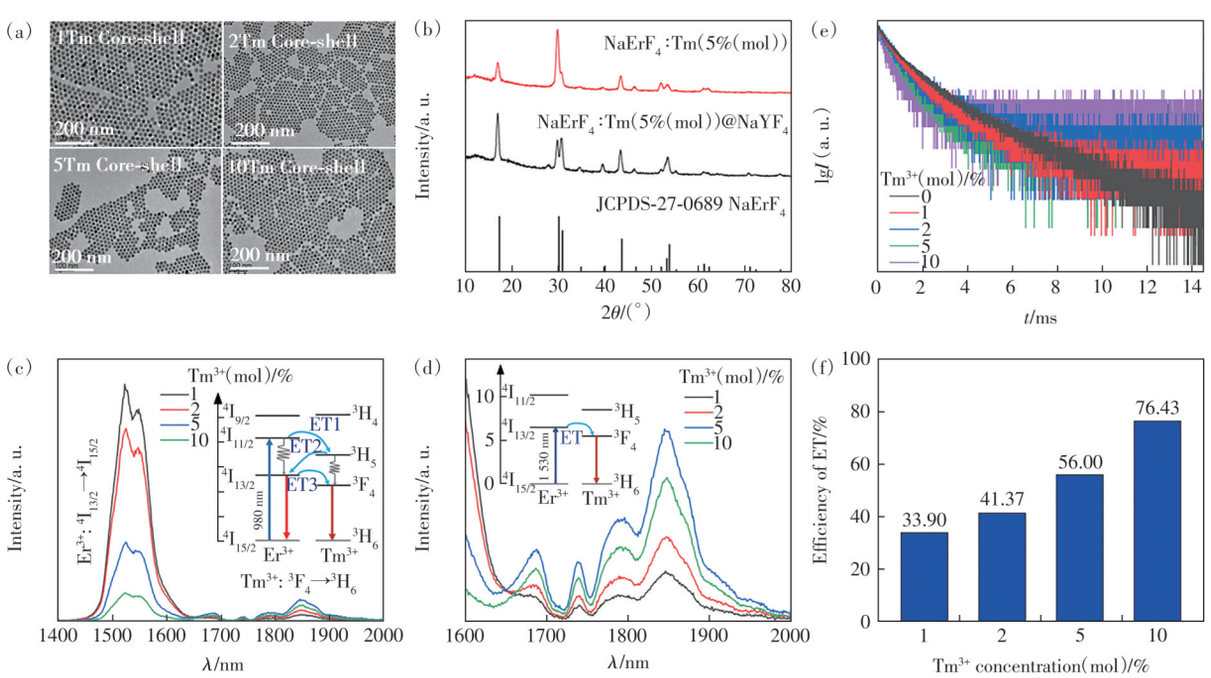

Fig. 2 (a)TEM images of $NaErF_4$:Tm(1%–10%)@$NaYF_4$ core-shell nanoparticles. (b)XRD patterns of $NaErF_4$:Tm(5%) core and $NaErF_4$:Tm(5%)@$NaYF_4$ core-shell nanoparticles. The standard JCPDS card of hexagonal $NaErF_4$ is also presented. Emission spectra of $NaErF_4$:Tm(1%–10%)@$NaYF_4$ core-shell nanoparticles under 980 nm(c) and 1 530 nm(d) excitations (Insets show the energy transfer processes between Er^{3+} and Tm^{3+}). (e)Decay curves of Er^{3+} at the $^4I_{13/2}$ with Tm^{3+} concentrations. (f)Energy transfer efficiency from Er^{3+} to Tm^{3+}

sign (%) here denotes molar percentage concentration. Unless otherwise specified, all percent signs in the following text shall adhere to this definition. The XRD results verify the hexagonal phase of the samples with good crystalline property (Fig. 2(b)). As illustrated in Fig. 2(c), the emission of Tm^{3+} at 1.8 μm from its $^3F_4 \rightarrow {}^3H_6$ transition was observed under 980 nm excitation, which depends closely on the doping concentration. The initial increase in Tm^{3+} emission with lifting concentration can be understood by an increase of $Er^{3+} \rightarrow Tm^{3+}$ energy transfer. This is in accordance with the decrease of Er^{3+} 1.5 μm emission during this process. The decline in emission observed at much higher Tm^{3+} content (>5%) may be due to the occurrence of concentration quenching. Under 980 nm excitation, there exists a cascade energy transfer from Er^{3+} ($^4I_{11/2}$) to Tm^{3+} ($^3H_5$) and Er^{3+} ($^4I_{13/2}$) and then Tm^{3+} ($^3F_4$)[23]. The non-radiative relaxation from $^3H_5$ also helps the population of Tm^{3+} at $^3F_4$ (Fig. 2(c)). Similar results were observed under 1 530 nm excitation (Fig. 2(d)), suggesting new excitations for NIR emissions. To reveal the specific energy transfer from Er^{3+} to Tm^{3+}, we further measured the lifetime of Er^{3+} at its $^4I_{13/2}$ energy level under pulsed 1 530 nm excitation (Fig. 2(e)). It shows a decrease from 3.48 ms to 0.82 ms with increasing Tm^{3+} concentrations from 0 to 10%, further confirming the occurrence of energy transfer from Er^{3+} to Tm^{3+} (Tab. S1), and the energy transfer efficiency from Er^{3+} to Tm^{3+} can reach 76.43% when Tm^{3+} is 10% (Fig. 2(f)).

In order to realize broadband NIR luminescence, the Ho^{3+} ions were further introduced in the sample by preparing the $NaErF_4$: Tm/Ho(5/0–10%)@$NaYF_4$ core-shell nanoparticles. As shown in Fig. 3(a), typical emission band of Ho^{3+} at 2.0 μm under 980 nm excitation was observed, showing an initial increase and then a drop in luminescence intensity with Ho^{3+} doping concentrations. The emissions of Er^{3+} and Tm^{3+} exhibit a decrease during this process (Fig. 3(b)). The luminescence behavior under 1 530 nm excitation is similar to that under 980 nm excitation (Fig. 3(c)–(d)). When the doping concentration of Ho^{3+} is 0.5%, its 2.0 μm emission intensity is comparable to that of the 1.8 μm emission of Tm^{3+}. This is important for the broadband NIR emission. However, the emission of Tm^{3+} shows a decrease under both 980 nm and 1 530 nm excitations, implying that there would exist another energy transfer channel between Tm^{3+} and Ho^{3+}, namely Tm^{3+} ($^3F_4$)→Ho^{3+} ($^5I_7$). To check it, we measured the lifetime of the $^3F_4$ energy level of Tm^{3+} under pulsed

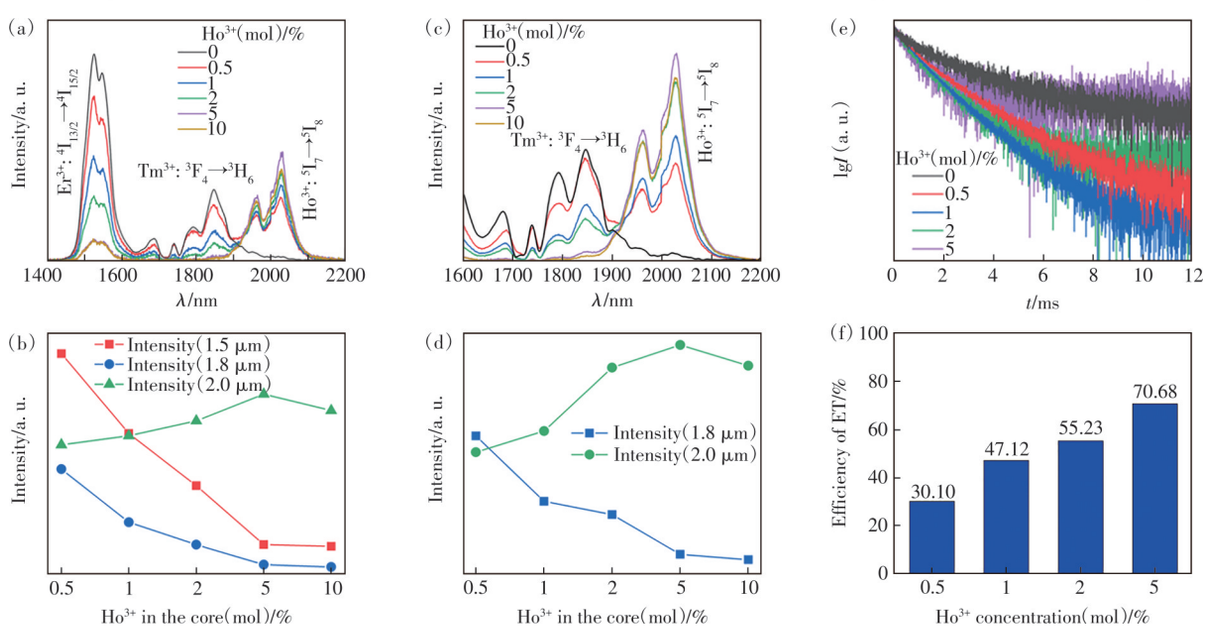

Fig. 3 Emission spectra of $NaErF_4$: Tm/Ho(5/0–10%)@$NaYF_4$ samples under 980 nm(a) and 1 530 nm(c) excitations. (b), (d)Dependence of the NIR emission intensities on Ho^{3+} concentrations for (a) and (c) samples. (e)Decay curves of Tm^{3+} at the $^3F_4$ state with different Ho^{3+} concentrations under 1 530 nm excitation. (f)Energy transfer efficiency from Tm^{3+} to Ho^{3+}

1 530 nm excitation. As shown in Fig. 3(e) and Tab. S2, it indeed shows a decrease from 3.82 ms to 1.12 ms with increasing Ho^{3+} doping concentration. The energy transfer efficiency also shows an increase during this process (Fig. 3(f)). It is worth noting that Ho^{3+} can also be activated by Er^{3+} directly, because the presence of Ho^{3+} results in a further decrease of the lifetime of Er^{3+} at $^4I_{13/2}$ (Fig. S3). Although the presence of Tm^{3+} helps bridge the energy gap between Er^{3+} ($^4I_{13/2}$) and Ho^{3+} ($^5I_7$) with enhanced 2.0 μm luminescence of Ho^{3+}, it also results in a quenching of the NIR emission of Tm^{3+}.

We next aimed to enhance the broadband NIR emissions of the samples by controlling the interactions between activators. As shown in Fig. 3(a) and Fig. 3(c), the presence of Tm^{3+} and Ho^{3+} in Er sublattice caused detrimental decline of the emission intensity of Tm^{3+}. This means that Tm^{3+} can also transfer energy to Ho^{3+} in addition to the sensitizer Er^{3+}. In this case, a spatial separation of Tm^{3+} and Ho^{3+} in two shell layers may help minimize such energy loss, as illustrated in Fig 4(a). Here, we designed and synthesized the control samples of $NaErF_4$:Tm(5%)@$NaErF_4$:Ho(0.5%)@$NaYF_4$ and $NaErF_4$:Tm/Ho (5%/0.5%) @$NaYF_4$ samples. As expected, the former sample indeed shows much better Tm^{3+} emission intensity with around 2-fold enhancement by comparison to the latter sample (Fig. 4(b)). This result demonstrates the advantage of core-shell engineering to amplify emission intensity by suppressing the unwanted quenchable interactions.

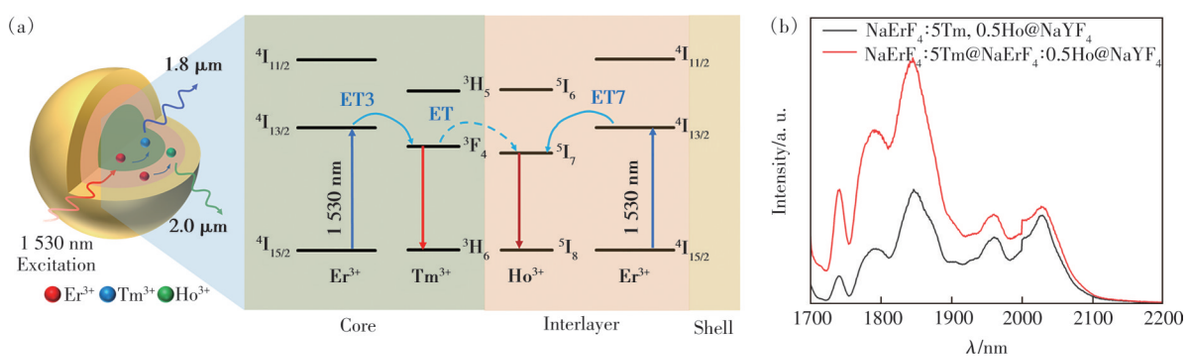

Fig. 4　(a)Schematic of core-shell-shell structure to depress cross talk between Tm^{3+} and Ho^{3+}. (b)Emission spectra of $NaErF_4$:Tm/Ho(5%/0.5%)@$NaYF_4$ and $NaErF_4$:Tm(5%)@$NaErF_4$:Ho(0.5%)@$NaYF_4$ nanoparticles under 1 530 nm excitation

It has been well recognized that Yb^{3+} is a good sensitizer to activate lanthanide emitters upon 980 nm excitation. To further enhance the broadband NIR emission of the samples under 980 nm excitation, the $NaYbF_4$ interlayer was inserted in the sample (Fig. 5(a)) to enhance the absorption of 980 nm excitation due to its $^2F_{5/2}$←$^2F_{7/2}$ absorption transition followed by the energy transfer to Er^{3+} ($^4I_{11/2}$)[14]. Subsequently, various energy transfer channels from Er^{3+} to Tm^{3+} and Ho^{3+} lead to their NIR emissions. For this purpose, we designed and synthesized the control samples of $NaErF_4$:Tm/Ho(6%/1%)@$NaYbF_4$@$NaYF_4$ core-shell-shell and $NaErF_4$:Tm/Ho(6%/1%)@$NaYF_4$ core-shell nanoparticles. Interestingly, the NIR emission from the sample with $NaYbF_4$ interlayer is greatly enhanced with around three showing an initial increase and then in comparison to the control sample without $NaYbF_4$ interlayer (Fig. 5(b)). The quantum yield of the 1.5 μm emission of this core-shell-shell sample is 13.94%, under 980 nm excitation with a power density of 51.6 W/cm^2, comparable to previous report[24]. This result confirms that adding the $NaYbF_4$ interlayer is an effective strategy to enhance the broadband NIR emission intensity by increasing the absorption of 980 nm excitation irradiance.

Similarly, since Er^{3+} is also responsive to the 808 nm excitation wavelength, we also attempted to enhance the NIR emissions under this excitation by designing the $NaErF_4$:Tm/Ho@$NaYbF_4$@$NaYF_4$:Yb/Nd core-shell-shell nanostructure(Fig. 5(c)). Here Nd^{3+} was incorporated into the outer shell layer as an additional sensitizer to enhance the absorption of the 808 nm excitation laser with subsequent energy transfer to Yb^{3+}[25]. Note that the $NaYbF_4$ interlayer not only

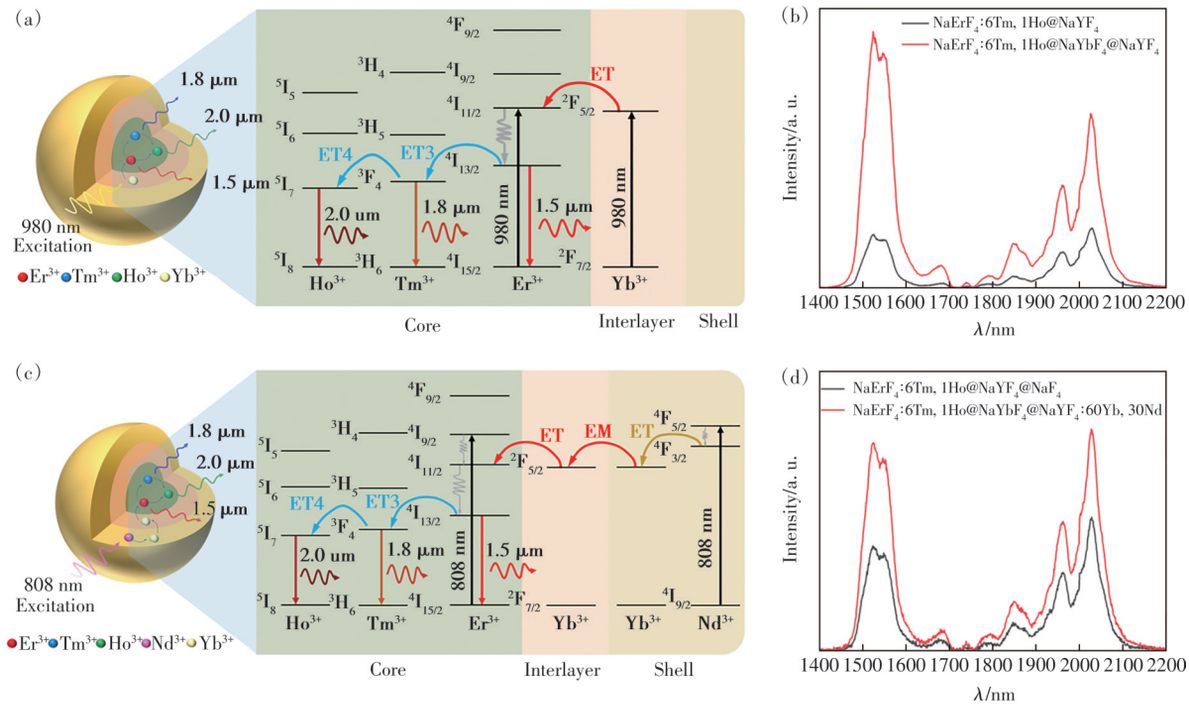

Fig. 5 (a) Schematic of introducing Yb-interlayer for enhancing NIR emissions in the $NaErF_4$: Tm/Ho (6%/1%) @$NaYbF_4$@$NaYF_4$ core-shell-shell nanostructure under 980 nm excitation. (b) Emission spectra of (a) sample and $NaErF_4$: Tm/Ho (6%/1%) @$NaYF_4$ under 980 nm excitation. (c) Schematic of introducing Nd/Yb-shell for enhancing NIR emissions in the $NaErF_4$: Tm/Ho@$NaYbF_4$@$NaYF_4$: Yb/Nd core-shell-shell nanostructure under 808 nm excitation. (d) Emission spectra of (c) sample and $NaErF_4$: Tm/Ho(6%/1%)@$NaYbF_4$@$NaYF_4$ under 808 nm excitation

serves as an energy migration channel to support energy flux but also helps reduce non-radiative processes between the lanthanide dopants in core and in the outer shell region, since the codoping of Nd^{3+} and Er^{3+} usually resulted in serious quenching of the emissions of Er^{3+}. Finally, it should be noted that suitable concentration of Nd^{3+} (*e. g.*, 30%) was adopted to suppress the concentration quenching caused by cross-relaxation[21]. Another important issue lies in the codoping of Yb^{3+} in the outmost shell layer, which can facilitate the energy transfer from Nd^{3+} to Yb^{3+} across the interfacial region. As expected, the NIR luminescence exhibited a nearly two-fold enhancement when compared to the sample without the Nd^{3+}/Yb^{3+} in the outermost shell (Fig. 5 (d)). The bright broadband NIR emission in nanoparticles under 808 nm excitation is important for biological imaging[26].

4 Conclusion

In conclusion, we have demonstrated a new design to realize broadband NIR emissions in lanthanide doped nanoparticles. By using Er sublattice as the sensitizing host to absorb the external excitation energy, effective NIR luminescence of Er^{3+}, Tm^{3+}, and Ho^{3+} was realized under multiple excitations at 808, 980, 1 530 nm. Moreover, the Yb^{3+} and Nd^{3+} were further introduced with suitable nanostructures to enhance the absorption at 980 nm and 808 nm, respectively, resulting in further enhanced NIR emissions at these two excitation wavelengths. These observations confirm that there exist efficient energy transfer channels between Er^{3+}, and Tm^{3+} and Ho^{3+} to achieve their NIR emissions. Our results present deep insight into the design of broadband NIR luminescent nanoparticles, which is contributable to frontier applications such as optical communication, night-vision devices, and biological imaging.

Supplementary Information and Response Letter are available for this paper at:http://cjl.lightpublishing.cn/thesisDetails#10.37188/CJL.20250055

References:

[1] FENG X, LIN L T, DUAN R, *et al.* Transition metal ion activated near-infrared luminescent materials [J]. *Prog. Mater. Sci.*, 2022, 129: 100973.

[2] HUANG W T, RAJENDRAN V, CHAN M H, *et al.* Near-infrared windows I and II phosphors for theranostic applications: spectroscopy, bioimaging, and light-emitting diode photobiomodulation [J]. *Adv. Opt. Mater.*, 2023, 11(11): 2202061.

[3] WEI D, XIA H P, FANG L Z, *et al.* Mg^{2+}-modified $LiBaF_3$: Ni^{2+} perovskite single crystals with broadband long wavelength near-infrared emission for imaging human vascular structures [J]. *Inorg. Chem. Front.*, 2024, 11(23): 8339-8349.

[4] WANG J T, GONG C S, YANG S H, *et al.* Cr^{3+} activated $Na_3RESi_3O_9$ (*RE* = Y, Lu, Sc) silicate broadband near-infrared phosphors for luminescence towards NIR-Ⅱ region *via* a multi-site occupancy strategy [J]. *J. Rare Earths*, 2024, 42(8): 1447-1457.

[5] ZHOU X F, GENG W Y, LI J Y, *et al.* An ultraviolet-visible and near-infrared-responded broadband NIR phosphor and its NIR spectroscopy application [J]. *Adv. Opt. Mater.*, 2020, 8(8): 1902003.

[6] 宋宏伟, 周东磊, 白雪, 等. 稀土掺杂铅卤钙钛矿发光、光电材料与器件研究进展 [J]. 发光学报, 2023, 44(3): 387-412.
SONG H W, ZHOU D L, BAI X, *et al.* Advances in rare earth doped lead halide perovskite luminescence, optoelectronic materials and devices [J]. *Chin. J. Lumin.*, 2023, 44(3): 387-412. (in Chinese)

[7] WEI Y R, YANG X D, MA Y R, *et al.* Lanthanide-doped nanoparticles with near-infrared-to-near-infrared luminescence for bioimaging [J]. *Chin. J. Chem.*, 2016, 34(6): 558-569.

[8] CHEN W W, HUANG X J, DONG Q, *et al.* Tunable ultra-broadband multi-band NIR emission in Bi-doped aluminogermanate glasses and fibers *via* controllable Al_2O_3 content for broadband amplifiers [J]. *J. Mater. Chem.* C, 2024, 12(2): 459-467.

[9] YANG Y W, CHEN Y, PEI P, *et al.* Fluorescence-amplified nanocrystals in the second near-infrared window for *in vivo* real-time dynamic multiplexed imaging [J]. *Nat. Nanotechnol.*, 2023, 18(10): 1195-1204.

[10] FENG Z G, XIA H P, WANG C, *et al.* 1.8 μm luminescent properties and energy transfer of Yb^{3+}/Tm^{3+} co-doped α-$NaYF_4$ single crystals [J]. *J. Alloy. Compd.*, 2016, 680: 26-30.

[11] LIU Q H, TIAN Y, WANG C Z, *et al.* Different dominant transitions in holmium and ytterbium codoped oxyfluoride glass and glass ceramics originating from varying phonon energy environments [J]. *Phys. Chem. Chem. Phys.*, 2017, 19(44): 29833-29839.

[12] BAI G X, TAO L L, LI K F, *et al.* Enhanced ~2 μm and upconversion emission from Ho-Yb codoped oxyfluoride glass ceramics [J]. *J. Non-Cryst. Solids*, 2013, 361: 13-16.

[13] ZHOU B, SHI B Y, JIN D Y, *et al.* Controlling upconversion nanocrystals for emerging applications [J]. *Nat. Nanotechnol.*, 2015, 10(11): 924-936.

[14] LIU S B, YAN L, HUANG J S, *et al.* Controlling upconversion in emerging multilayer core-shell nanostructures: from fundamentals to frontier applications [J]. *Chem. Soc. Rev.*, 2022, 51(5): 1729-1765.

[15] HUANG J S, YAN L, LIU S B, *et al.* Expanding the toolbox of photon upconversion for emerging frontier applications [J]. *Mater. Horiz.*, 2022, 9(4): 1167-1195.

[16] YAO Y H, ZHANG S A, ZHANG H, *et al.* Laser polarization and phase control of up-conversion fluorescence in rare-earth ions [J]. *Sci. Rep.*, 2014, 4: 7295.

[17] GIANG L T K, TREJGIS K, MARCINIAK L, *et al.* Fabrication and characterization of up-converting β-$NaYF_4$: Er^{3+}, Yb^{3+}@$NaYF_4$ core-shell nanoparticles for temperature sensing applications [J]. *Sci. Rep.*, 2020, 10(1): 14672.

[18] LI X M, ZHANG F, ZHAO D Y. Lab on upconversion nanoparticles: optical properties and applications engineering *via* designed nanostructure [J]. *Chem. Soc. Rev.*, 2015, 44(6): 1346-1378.

[19] LI Y Y, ZHANG P S, NING H R, *et al.* Emitting/sensitizing ions spatially separated lanthanide nanocrystals for visualizing tumors simultaneously through up-and down-conversion near-infrared Ⅱ luminescence *in vivo* [J]. *Small*, 2019, 15(51): 1905344.

[20] CHANG Y L, CHEN H R, XIE X Y, *et al.* Bright Tm^{3+}-based downshifting luminescence nanoprobe operating around

1 800 nm for NIR-IIb and c bioimaging [J]. *Nat. Commun.*, 2023, 14(1): 1079.

[21] SHENG W, HUANG J S, CAI Z Y, *et al*. Multi-wavelength excitable mid-infrared luminescence and energy transfer in core-shell nanoparticles for nanophotonics [J]. *Nanoscale*, 2023, 15(13): 6313-6320.

[22] ZHOU B, YAN L, HUANG J S, *et al*. NIR II-responsive photon upconversion through energy migration in an ytterbium sublattice [J]. *Nat. Photonics*, 2020, 14(12): 760-766.

[23] HU Z Y, HUANG J S, YAN L, *et al*. Enhancing NIR-Ⅱ luminescence of erbium sublattice through lanthanide-mediated energy modulation [J]. *Optik*, 2022, 259: 169037.

[24] FISCHER S, BRONSTEIN N D, SWABECK J K, *et al*. Precise tuning of surface quenching for luminescence enhancement in core-shell lanthanide-doped nanocrystals [J]. *Nano Lett.*, 2016, 16(11): 7241-7247.

[25] CHEN Y, TAN J C, ZHANG P X, *et al*. Influence of Nd^{3+} concentration on mid-infrared emission in PbF_2 crystal co-doped with Ho^{3+} and Nd^{3+} ions [J]. *J. Rare Earths*, 2024, 42(3): 479-487.

[26] CHANG H, HUR W, KANG H, *et al*. *In vivo* surface-enhanced Raman scattering techniques: nanoprobes, instrumentation, and applications [J]. *Light Sci. Appl.*, 2025, 14(1): 79.

赵宇(2000-),男,河南郑州人,硕士研究生,2022年于北京化工大学获得学士学位,主要从事稀土发光纳米材料的研究。

E-mail: zydmmjd@foxmail.com

周博(1982-),男,山东临沂人,博士,教授,博士生导师,2011年于中国香港城市大学获得博士学位,主要从事发光机理、稀土发光材料及光电器件领域的研究。

E-mail: zhoubo@scut.edu.cn